

Direct inelastic scattering of nitric oxide from clean Ag(111): Rotational and fine structure distributions

G. D. Kubiak, J. E. Hurst, Jr.,^{a)} H. G. Rennagel,^{b)} G. M. McClelland,^{c)} and R. N. Zare

Department of Chemistry, Stanford University, Stanford, California 94305
(Received 17 June 1983; accepted 4 August 1983)

The internal state distribution of scattered NO is determined by laser fluorescence excitation spectroscopy when a pulsed, supersonically cooled beam of NO is incident upon the (111) face of a clean Ag single crystal. It is found that the mean rotational energy $\langle E_r \rangle$ depends linearly on the surface temperature $E_s (= T_s)$ and the incident kinetic energy normal to the surface E_n according to $\langle E_r \rangle = a(E_n + \langle E'_w \rangle) + bE_s$. The three parameters a , b , and $\langle E'_w \rangle$ are constants independent of E_n and E_s . Arguments are presented showing that $\langle E'_w \rangle$ is some measure of the average NO/Ag(111) well depth. For the $\Omega = 1/2$ fine structure component we estimate that $\langle E'_w \rangle = 2850 \pm 450$ K (245 ± 40 meV), $a = 0.88 \pm 0.009$, and $b = 0.18 \pm 0.04$ while for $\Omega = 3/2$, $\langle E'_w \rangle = 2080 \pm 150$ K (180 ± 13 meV), $a = 0.132 \pm 0.005$, and $b = 0.11 \pm 0.02$. The results are compared to the predictions of one-dimensional impulsive models of gas-surface scattering. These models are able to describe qualitatively the dependence of $\langle E_r \rangle$ on E_n and E_s but only when trapping fractions that are incompatible with experiment are predicted simultaneously.

I. INTRODUCTION

Dynamical studies have played an expanded role recently in elucidating the pertinent forces which govern the interaction between a gas molecule and a solid surface. The subject of extensive reviews,¹⁻³ low pressure studies of gas-surface dynamics had until 1981 concentrated solely on the center-of-mass (c. m.) motion of the scattered or desorbed particles. Although the characterization of the c. m. motion has been very fruitful for atomic systems,⁴⁻⁶ translation is but one degree of freedom among many in molecular systems. Since the determination of the distributions over all molecular degrees of freedom is crucial to our understanding of molecular interactions with surfaces, it is not surprising that this has been the goal of many recent efforts in the field. These include the determination of rotational and/or vibrational distributions of NO,⁷⁻¹² H₂(D₂),¹³ HD,¹⁴ HF,¹⁵ CO,¹⁶ and I₂¹⁷ scattered from a variety of metallic and insulator surfaces and NO,¹⁸ CO₂,¹⁹⁻²¹ OH,²² and N₂²³ desorbing from transition metal crystal surfaces or polycrystalline foils.

With the exception of H₂, HD, and NO at high incident kinetic energy, all surface-scattered molecular rotational distributions reported to date for clean surfaces are Boltzmann in form and yield rotational temperatures T_r , which are generally less than or equal to the surface temperature T_s . However, as we will show, in cases where trapping followed by desorption is not the dominant scattering mechanism, information regarding the gas-surface potential may be extracted even when rotational distributions appear to be described by a single temperature T_r .

There have been two previous studies of the final in-

ternal state distributions of NO scattered from clean Ag(111).^{8,9} In a previous publication⁸ we reported that when an effusive, room temperature beam of NO impinging on Ag(111), the scattered molecules were characterized by a Boltzmann distribution of rotational states. The resulting rotational temperature was less than the surface temperature, and the measured rotational temperatures varied weakly with T_s . Integration over both incident and exit scattering angles prevented the unambiguous determination of the dominant scattering mechanism. In an independent study of the same system, Kleyn, Luntz, and Auerbach⁹ determined that for incident kinetic energies ≥ 3724 K the NO distribution of rotational states exhibited both Boltzmann and non-Boltzmann regions for low and high rotational quantum numbers (J), respectively. The non-Boltzmann fraction contained a broad maximum for high incident kinetic energies and was tentatively interpreted as a rotational population rainbow. Rotational polarization was observed to occur for states within this broad rainbow but not for rotational states below or above it. At high incident kinetic energies and high J , preferential population of one of the NO Λ doublets and J -dependent exit angular distributions were also noted.

In the present study, we report measurements of the rotational state and electronic fine structure distributions of NO scattered from clean Ag(111). We use the technique of laser fluorescence excitation spectroscopy to extract internal state populations of molecules produced by a pulsed supersonic expansion and scattered from the sample crystal in ultrahigh vacuum (UHV). We report measurements of the NO rotational populations vs incident angles and surface temperature at a variety of incident kinetic energies. We also discuss the prevalent excitation of the NO $^2\Pi_{3/2}$ state which lies 123 cm⁻¹ above the ground $^2\Pi_{1/2}$ fine structure component and compare this excitation to that found in gas-phase NO/Ar collisions.²⁴ The current effort differs from that of Kleyn *et al.*⁹ in that our measurements cover the range of incident total kinetic energies from 338 to 2321

^{a)} Present address: IBM Thomas J. Watson Research Center, P. O. Box 218, Yorktown Heights, NY 10598.

^{b)} Present address: Department of Chemistry, U. S. Military Academy, West Point, NY 10996.

^{c)} Present address: Department of Chemistry, Harvard University, 12 Oxford Street, Cambridge, MA 02138.

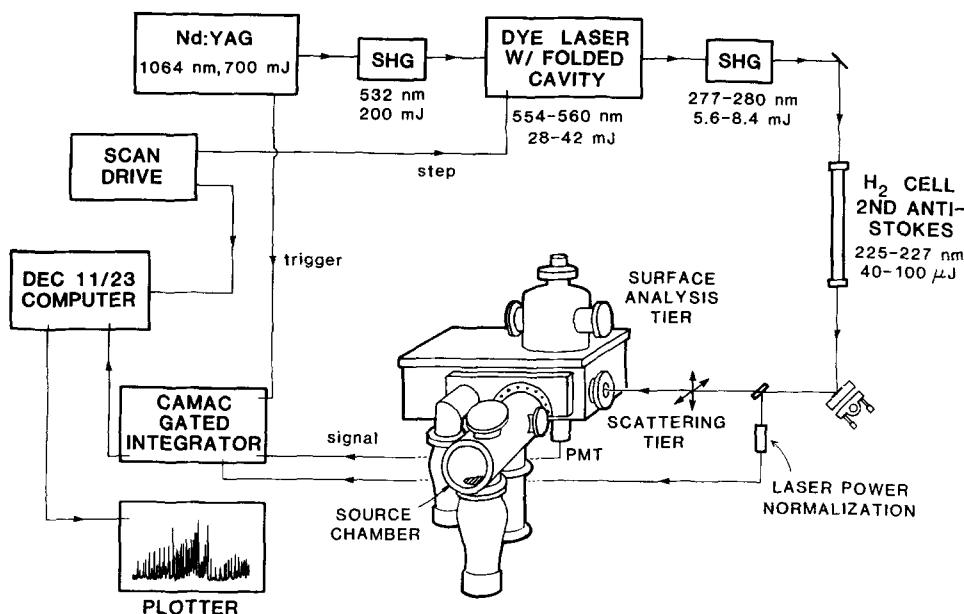


FIG. 1. Overall schematic of experiment.

K (surface normal component E_n from 169 to 2321 K) compared with the range of 3724 to 11 636 K (E_n from 2211 to 10 821 K). In addition, the method of rotational population analysis is considerably different; no separation is made in our treatment between the Boltzmann and non-Boltzmann regions.

The remainder of this paper is organized in three parts. The next section describes the details of the experimental arrangement: the scattering apparatus; the molecular beam source; the laser excitation and fluorescence collection methods; and the Ag(111) crystal preparation, respectively. Section III reports the experimental results and Sec. IV discusses these results and compares them to predictions of a one-dimensional impulsive model for rotationally inelastic scattering.

II. EXPERIMENTAL

Figure 1 shows a schematic diagram of the overall experimental arrangement. The apparatus consists of a stainless steel UHV chamber pumped by turbomolecular or trapped oil diffusion pumps, a triply differentially pumped pulsed supersonic beam source, a laser excitation source and associated steering and focusing optics, and, finally, signal fluorescence collection, amplifying, and averaging devices. The scattering sample surface is first characterized by low energy electron diffraction (LEED) and Auger electron spectroscopy (AES) and, when necessary, cleaned either by Ar^+ ion bombardment or chemical oxidation/reduction. Following surface preparation, the sample is placed along the molecular beam axis and inclined at the appropriate scattering angle. The incident NO beam is produced by expansion through a repetitively pulsed nozzle having a stagnation pressure and nozzle diameter of 5 atm and 500 μm , respectively. The beam is skimmed and collimated during its passage through two differentially pumped buffer regions and strikes the crystal 19.2 cm after it leaves the nozzle orifice. The scattered molecules are probed by

a suitably delayed pulsed laser which is mildly focused and which is scanned in excitation wavelength between 224.0–227.0 nm to excite the (0, 0) band of the $\text{NO } A^2\Sigma^+ - X^2\Pi_{1/2,3/2}$ transition (the NO γ band system). The probed scattering angle is selected by varying the position of the laser beam with respect to the surface. The resulting total molecular fluorescence is collected by $f1.4$ optics and imaged onto the photocathode of a photomultiplier (PMT). The fluorescence is monitored as a function of excitation frequency using gated integration and signal averaging until the signal-to-noise ratio is at least 20 for a typical rotationally resolved spectral line.

A. Apparatus

The UHV scattering chamber, shown in cross section in Fig. 2, is evacuated by a 1500 ls^{-1} turbomolecular pump (Leybold-Heraeus) whose foreline is pumped by a water-baffled 2 in. diffusion pump. The chamber has a typical base pressure of 2×10^{-10} Torr following a mild 125 $^\circ\text{C}$ bakeout. We have also used a liquid-nitrogen-trapped 10 in. oil diffusion pump to evacuate the chamber but its nominal base pressure is an order of magnitude higher due to inefficient trapping. Results presented here are independent of the pumping scheme employed. Bakeout heat is provided by three internal 1500 W quartz lamp heaters and assorted external contact strip heaters. The chamber is divided functionally into two levels. The upper tier contains the LEED gun and electron optics, retarding field AES, Ar^+ bombardment gun, and a sample overlayer gas doser. Sample manipulation and characterization are performed in this upper tier prior to a scattering experiment. Sample translation to the lower scattering tier of the apparatus is accomplished by a magnetically coupled manipulator having a 12 in. stroke. The angle of incidence can be set to within 5° by rotating the sample mounting and heating assembly about an axis approximately 2 cm behind the crystal face. Radiative sample heating is provided by a tungsten ribbon housed within a doubly radiation-

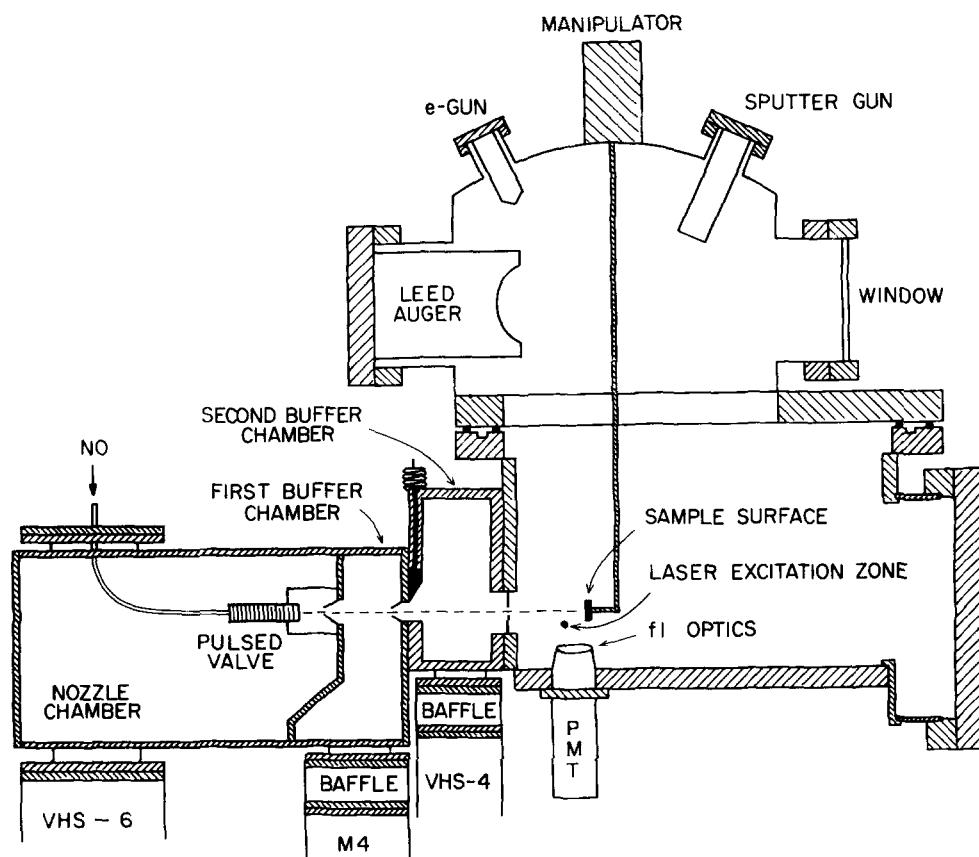


FIG. 2. Cross section of pulsed molecular beam source and surface analysis/scattering chambers.

shielded cylinder. The crystal is attached to one end of the cylinder with small tantalum tabs.

The lower tier of the apparatus contains a series of light traps and baffles to decrease scattered laser light. The laser enters the scattering region through a high surface quality quartz window, proceeds through the first light baffle, excites fluorescence in the interaction zone by passing perpendicular to the principal scattering plane, leaves this zone through a second light baffle, and strikes a beam dump constructed of two Corning 7-54 absorption filters. Although this arrangement does significantly reduce scattered light, the major reduction is accomplished by delaying the opening of the gated integrator until after the scattered laser light signal has become quiescent. This is possible because of the relatively long fluorescence lifetime of the NO A state, 180 ns.²⁵ The scattered NO is probed with the laser intersecting the molecules 7–14 mm from the surface. The fluorescence signal is collected by $f1.4$ quartz lenses situated 2.5 cm below the molecular beam and surface intersection and focused through a calcium fluoride window onto the partially masked cathode of a solar blind EMI G26H315 PMT. Two different gated integration systems were used to record the PMT output. One system employed a PAR 162 boxcar with dual 165 plug-ins whose outputs were stored and averaged in a Nicolet 1170 signal averager. The other used a CAMAC/computer system employing a combination of LeCroy (models 2323 delay timer and 2249 SG ADC gated integrator) and homebuilt modules. The digitized signals were then passed to a DEC 11/23 computer. Typically, five laser

shots are integrated at each wavelength increment before being stored. Repetitive excitation spectral scans are averaged to minimize any artifacts associated with long term drift of the molecular beam flux. Laser intensity and NO fluorescence signals are recorded for each laser shot in two separate channels. Subsequent ratioing corrects for laser intensity variations associated with the gain curve of the dye and shot-to-shot fluctuations. A suitable spectrum is obtained in approximately 45 min.

B. NO molecular beam source

The source beam of scattering gas is produced by the differentially pumped source chamber shown in Fig. 2. The sample gas expands from stagnation pressures (P_0) of 5 atm through a pulsed valve having a nozzle orifice (D) of 500 μm . The pulsed valve design is identical to that of Duncan and Byer,²⁶ so that details about its construction will not be given here. The nozzle operated at 9 J/pulse, and had a temporal pulse width of 100 μs FWHM at the crystal. Such pulse durations preclude velocity analysis of the scattered NO. Therefore the populations we report are averaged over velocity. The relaxed beam expands into a pressure of approximately 5×10^{-7} Torr but increases the expansion chamber pressure to 1×10^{-5} Torr during the pulse. Pumping in this stage is provided by a Varian VHS-6 diffusion pump having a Mexican hat cold cap. The beam is skimmed by a 2 mm skimmer situated 10 mm from the expansion orifice and enters the first buffer region. This first buffer stage, pumped by a water-baffled 4 in. diffusion

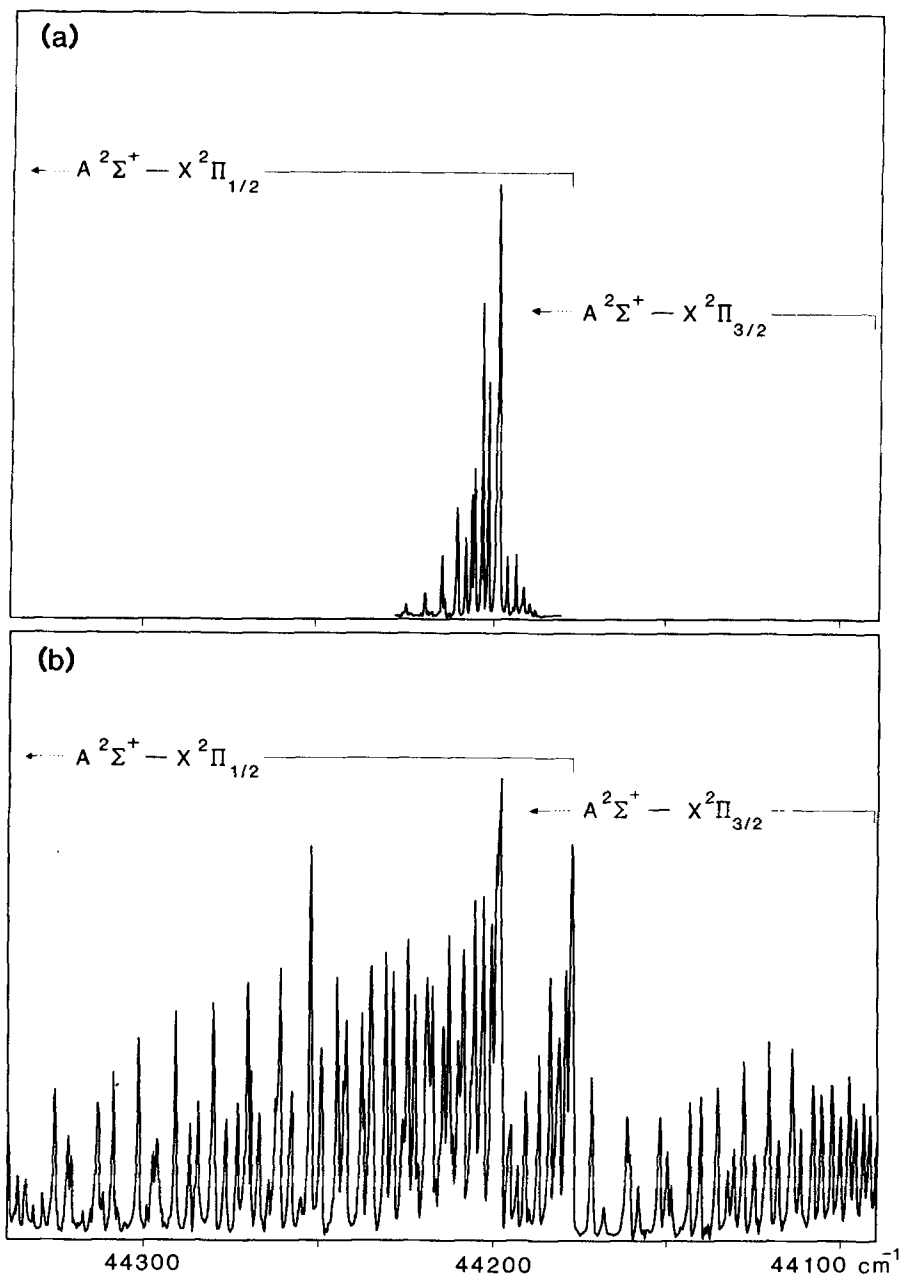


FIG. 3. Fluorescence excitation spectra of the NO $A^2\Sigma^+ - ^2\Pi_{1/2,3/2}(0,0)$ transition. (a) Spectrum of incident unseeded NO beam ($P_0 = 4$ atm, $d = 0.50$ mm) showing efficient rotational and fine structure component relaxation. The observed rotational temperature is 11 K. (b) NO spectrum after scattering from Ag(111) showing rotational and fine structure excitation. Conditions were $E_n = 557$ K, $\theta_i = 45^\circ$, $T_s = 650$ K, yielding a mean rotational energy of 375 K.

pump, has a beam-off pressure of 5×10^{-8} Torr, increasing to 1×10^{-7} Torr during the pulse. A second skimmer forms this region's exit orifice into the final buffer chamber. The latter is evacuated by a water-baffled VHS-4 diffusion pump and which attains a base pressure of 5×10^{-9} Torr, rising to a pulse-on value of 1.0×10^{-8} Torr. Final beam collimation is defined by a 1 mm orifice in the second buffer exit plate, resulting in a beam width of 1.5 mm at the crystal.

Backing pressures for the nozzle are provided directly from an NO supply tank having a quoted purity of 99% or from equilibrated seeding mixtures of 20% NO/80% Kr or 17% NO/83% He. Rotational relaxation in the beam was extremely efficient, as evidenced by the excitation spectrum shown in Fig. 3(a) and typically yielded rotational temperatures of 3–11 K. It should be mentioned, however, that the rotational distributions of the relaxed

beam deviate from a Boltzmann distribution by the presence of a high energy tail so that defining a rotational temperature is something of a misnomer. Relaxation of the $F_2 \Omega = 3/2$ fine structure component, which lies 123 cm^{-1} above the $F_1 \Omega = 1/2$ component of the $^2\Pi$ state, was also quite efficient. The ratio of the integrated fluorescence intensities for these two components yields an upper limit to the electronic temperature of 45 K. The translational temperature could not be measured directly, but from the expansion conditions and the measured rotational/electronic relaxation is calculated to be 3 K. Mean molecular velocities were determined from energy balance of the measured internal relaxation and the initial source stagnation temperature. For a pure NO beam, the velocity determined in this way was $7.89 \times 10^4 \text{ cm/s}$, which compares favorably with a mean velocity of $7.83 \times 10^4 \text{ cm/s}$ measured for expansion conditions²⁷ having lower $P_0 D$. Mixed rare gas/NO beam

velocities were determined from the measured delay between the nozzle firing trigger pulse and subsequent fluorescent pulse by assuming a fixed lag in time between the trigger pulse and the actual release of molecules from the valve orifice.

Attempts were made to find features in the NO beam excitation spectrum that could be identified with either $(\text{NO})_n$ polymers or, when seeding was employed, rare gas/NO van der Waals molecules. Previous mass spectrometric measurements of the total polymer fraction of NO beams produced under milder, continuous expansion conditions²⁷ suggest values of 10^{-3} – 10^{-2} . We take 10^{-3} as the lower limit to the total polymer fraction for our more vigorous expansion; van der Waals fractions are likely to be even higher²⁸ although still at a level which we believe to be insufficient to compromise the results presented here.

C. Laser excitation source

Laser excitation wavelengths were produced in the spectral region between 227.0–224.0 nm to excite the (0, 0) band of the $\text{NO } A^2\Sigma^+_{1/2} - X^2\Pi_{3/2,1/2}$ system. The second harmonic output of a Quanta-Ray DCR-1A pulsed Nd^{3+} :YAG laser was used to pump a slightly modified Quanta-Ray pulsed dye laser to produce 40 mJ pulses of tunable radiation near 558.0 nm having a time-averaged bandwidth of 0.2 cm^{-1} . Reduced bandwidth, and the resulting increase in spectral brightness, was achieved by incorporating a very simple cavity folding mirror of the Littman type.²⁹ The visible dye laser output was then frequency doubled in KDP and scanned with a commercial unit (Quanta-Ray WEX). Stimulated Raman scattering of the focused doubled radiation was produced in a cell containing 125 psi of H_2 gas; pulses having energies of $100 \mu\text{J}$ into a bandwidth of 0.5 – 0.7 cm^{-1} were routinely generated. The desired second anti-Stokes line was separated from all others with a quartz 60° dispersing prism. Unwanted dispersive effects such as beam walk were compensated with a second identical prism in a mirror image configuration to the first.

Excitation pulse energies used to record experimental spectra were deliberately reduced to $40 \mu\text{J}$ to avoid hazards associated with saturation. Pulse energy densities greater than $50 \mu\text{J}/\text{mm}^2$ exhibited clear indications of saturation in the low rotational levels populated in the NO beam and were manifested by a relative attenuation of fluorescence intensity from lines having large line strengths when compared with those having much weaker transition strengths (e.g., $^3R_{21}$ lines).

D. Crystal preparation

The sample crystal was prepared from a disk having a quoted purity of 99.999% and an orientation tolerance of 1° (Monocrystals, Inc.). Standard polishing techniques were employed, followed by chemical polishing in a dilute solution of KCN and H_2O_2 ³⁰ to obtain a mirror finish. *In situ* removal of contaminants such as carbon, oxygen, sulfur, and chlorine was accomplished by soft Ar^+ sputtering for 30 min at 400 eV and $0.75 \mu\text{A}/\text{cm}^2$. Surface temperatures during sputtering were 750–800 K

and remained at this elevated level for 2–5 min after bombardment until high contrast 1×1 LEED patterns were produced. Sample contamination with hydrocarbons during data acquisition was a problem only for the lowest surface temperature studied and was removed after each signal averaging period by applying the prescription above. Sample temperatures were measured with a Pt/Pt–10%Rh thermocouple mounted in a 0.6 mm hole drilled in the side of the crystal. The temperature measurements were underestimated by at most 3% because of incomplete contact between the thermocouple and the sample.

III. RESULTS

A. Rotational excitation

Figure 3 shows typical fluorescence excitation spectra of the incident NO beam [Fig. 3(a)] and of the scattered molecules [Fig. 3(b)]. Whereas the NO internal state distribution from the supersonic expansion is rotationally cold ($T_r = 11 \text{ K}$) and almost entirely in the lowest $^2\Pi_{1/2}$ fine structure component, that from the surface shows extensive rotational and fine structure excitation. These spectra are obtained as follows. First we subtract that fraction of the averaged laser intensity spectrum which results in a zeroed fluorescence spectrum baseline. This is done to account for the small amount of scattered laser light which persists into the fluorescence gating period. The resulting spectrum is then divided by the laser intensity data to normalize it with respect to laser power and to minimize the effects of the large pulse-to-pulse variations typical of the stimulated Raman cell output.

The measured peak height for each assigned and fully resolved line is divided by its corresponding calculated rotational line strength³¹ and the logarithm of this quantity is plotted against the rotational term energy of that state. A representative result, which we call a Boltzmann plot, is shown in Fig. 4. As in all laser excitation techniques, the resulting signal is proportional to density and not flux.

Five features are evident in Fig. 4: (1) The points corresponding to the three lowest values of the perpendicular component of the incident molecular kinetic energy E_n have a linear dependence in this plot for both the $\Omega = 1/2$ and $\Omega = 3/2$ components, which is to say that the distributions are Boltzmann and that the rotational degree of freedom can be characterized by a temperature. (2) The points for $E_n = 2321 \text{ K}$ (200 meV) deviate at high J from this linear, or Boltzmann, dependence and exhibit a broad maximum which has been identified as a rotational rainbow.⁹ Because the rotational distributions are not in all cases Boltzmann, we introduce the mean final rotational energy, denoted by $\langle E_r \rangle$, as a measure of the rotational excitation caused by collision with the surface. This mean rotational energy is equal to T_r when the distribution is Boltzmann. (3) The $\langle E_r \rangle$ values obtained from the distributions for the $\Omega = 3/2$ component are generally higher than their $\Omega = 1/2$ counterparts (see Table I). This has previously been seen.^{9(c)} (4) As evidenced by the intercepts, the $\Omega = 1/2$ component is more populated than the $\Omega = 3/2$ component

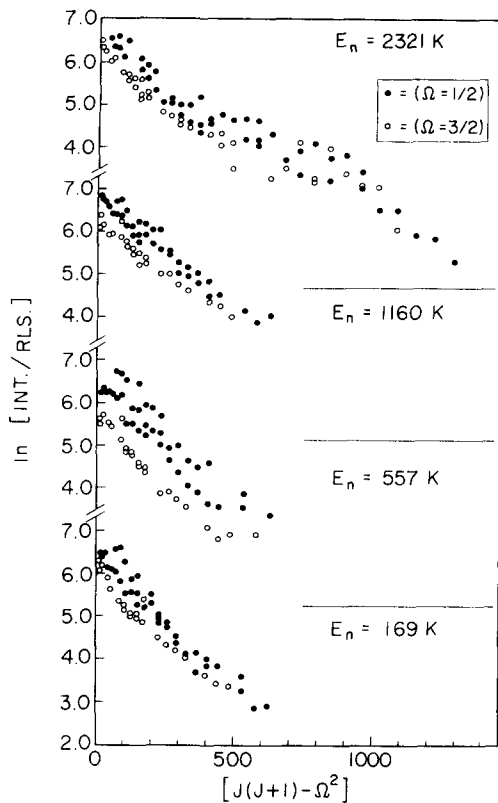


FIG. 4. Boltzmann plots of the rotational state distributions measured within each fine structure component at four different E_n values and fixed $T_s = 650$ K. Full and open circles correspond to $\Omega = 1/2$ and $\Omega = 3/2$ states, respectively. The energy scale is that appropriate to rotational energies in a strict Hund's case (a) angular momentum coupling scheme. Multiple points at the same energy correspond to populations determined from different rotational branches.

although there is substantial excitation of the latter. (5) The branches corresponding to the different orientations of the NO π cloud with respect to the plane of rotation (Λ components) have identical population within the uncertainty of the data.

To probe the effect of incident molecular kinetic energy and surface temperature on the rotational excita-

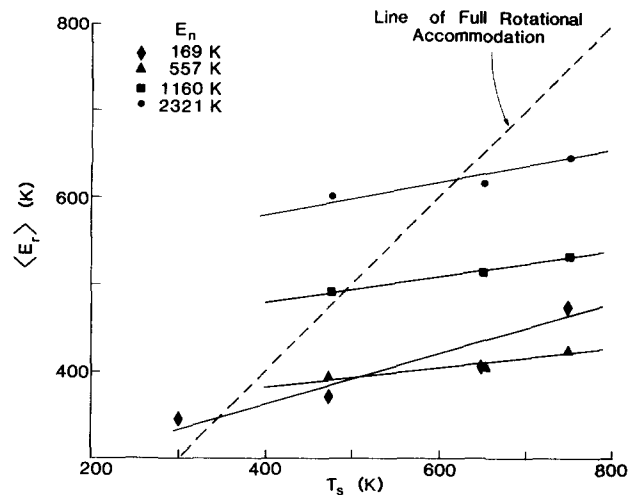


FIG. 5. Plot of the mean rotational energy averaged over both spin-orbit components vs the surface temperature at four values of E_n . See Table I for the values of $\langle E_r \rangle$ corresponding to each individual spin-orbit component. Note the obvious trend of increasing $\langle E_r \rangle$ with increasing E_n . The line of full rotational accommodation is that for which $\langle E_r \rangle = T_s$.

tion, we have determined $\langle E_r \rangle$ as a function of surface temperature for four separate values of E_n , the component of the incident kinetic energy projected along the surface normal. The four values of E_n were obtained by using different NO/rare gas mixtures and/or by adjusting the incident angle. The results, summarized in Table I, demonstrate that (1) $\langle E_r \rangle$ increases with T_s and (2) $\langle E_r \rangle$ increases with E_n for $E_n \geq 557$ K. To visualize these trends, we plot in Fig. 5 the values of $\langle E_r \rangle$ averaged over the two spin-orbit components vs the surface temperature T_s .

Although a plot such as Fig. 5 may seem the natural way to present the data, it masks an important contribution to the rotational excitation, namely, that made by the attractive potential between gas and surface. This is readily seen in Fig. 6, in which we plot the dimensionless variables $\langle E_r \rangle / E_n$ vs E_s / E_n , for each fine structure component, where we now define $E_s (= T_s)$ as the energy associated with the surface temperature.³² By varying independently the total incident kinetic energy

TABLE I. $\langle E_r \rangle$ computed for each fine structure component, $\Omega = 1/2 \equiv F_1$, $\Omega = 3/2 \equiv F_2$, tabulated for all surface temperatures ($T_s = E_s$) against the total incident kinetic energy, the incident angle, and the resulting normal component of the kinetic energy. Standard deviations are in parentheses.

E_i (K)	θ_i	E_n (K)	E_s (K)				
			300	475	650	750	
F_1	338	45°	169	320(10)	373(8)	407(9)	445(11)
F_2	338	45°	169	367(10)	397(11)	445(12)	504(17)
F_1	1114	45°	557		395(20)	404(16)	427(19)
F_2	1114	45°	557		392(15)	402(13)	431(14)
F_1	2321	45°	1160		484(10)	501(14)	520(14)
F_2	2321	45°	1160		503(12)	537(17)	550(18)
F_1	2321	0°	2321		537(25)	587(25)	583(29)
F_2	2321	0°	2321		632(20)	643(28)	662(26)

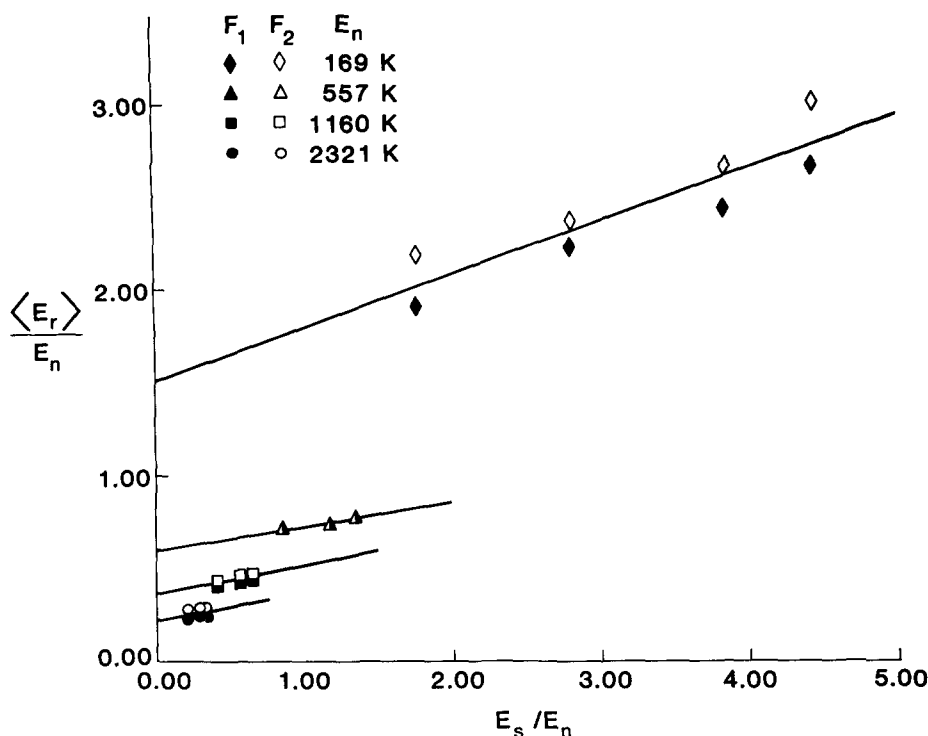


FIG. 6. Plot of the reduced variables, $\langle E_r \rangle / E_n$ vs E_s / E_n for the four values of E_n listed, where the open and closed symbols refer to the $\Omega = 3/2$ and $\Omega = 1/2$ components, respectively. The data for each E_n show a linear dependence of E_s with a different intercept.

E_i and θ_i at fixed E_s we find that $\langle E_r \rangle$ depends on both E_i and θ_i . We are motivated to use $E_n = E_i \cos^2 \theta_i$ because one might expect that the Ag(111) surface acts as a flat plane toward the incident NO, i. e., the NO/Ag(111) potential is approximately one dimensional. This is supported by He scattering studies³³ which have shown that this close-packed face has a corrugation depth of < 0.01 Å. In addition, calculations have shown³⁴ that the classical turning point of the scattering atom probed at the thermal energies used in typical scattering experiments is a sufficient distance away from the atomic cores that the modulation of the potential over the unit mesh is much less than that of the atomic cores themselves. These findings suggest that close-packed faces of crystalline metals will appear quite flat.

The result of constructing a plot of this form is that the data clearly separate into four distinct groups corresponding to the four values of E_n . In Fig. 6 we have drawn least squares linear fits to the $\langle E_r \rangle / E_n$ data averaged over the two fine structure components. These lines demonstrate that the data for $E_n \geq 557$ K have similar slopes but different intercepts. On closer inspection, each E_n group when taken individually shows an additional, though much smaller, splitting corresponding to the individual fine structure component behavior. Attempting to describe the plotted data by a single line, however, yields a much poorer fit and is therefore rejected.

An important result, which is based on the fact that the data form the family of parallel lines shown in Fig. 6, is that the data can be described by an equation of the form:

$$\langle E_r \rangle = a(E_n) E_n + b E_s, \quad (1)$$

where b is a constant, independent of E_n and E_s , and a is a parameter whose dependence on E_n has yet to be determined. To extract this dependence we plot in Fig. 7 the values of $\langle E_r \rangle$ against E_n at constant E_s . As can be seen, the data are well described by a line for $E_n \geq 557$ K, i. e.,

$$\langle E_r \rangle = a E_n + b(E_s) E_s. \quad (2)$$

Combining the results of Eqs. (1) and (2) we find that $\langle E_r \rangle$ obeys the bilinear expression:

$$\langle E_r \rangle = a E_n + b E_s + c, \quad (3)$$

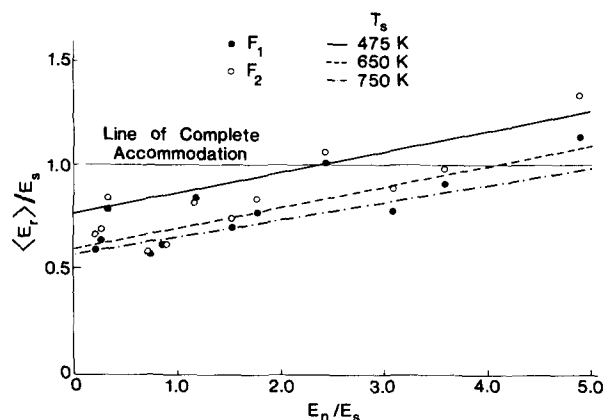


FIG. 7. Plot of the reduced variables, $\langle E_r \rangle / E_s$ vs E_n / E_s for the three values of E_s listed. As in previous tables the open and closed symbols refer to the $\Omega = 3/2$ and $\Omega = 1/2$ components, respectively. The data for each E_s show a linear dependence on E_n with a different intercept. The lines drawn are least squares fits to the $E_n \geq 557$ K data only.

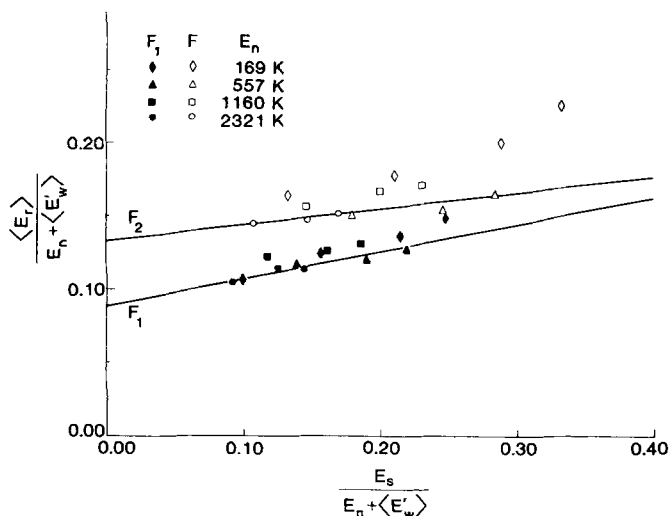


FIG. 8. Final plot of the reduced variable $\langle E_r \rangle / (E_n + \langle E'_w \rangle)$ vs $E_s / (E_n + \langle E'_w \rangle)$ for each spin-orbit component. As in earlier plots, only data for $E_n \geq 557$ K has been used in the bilinear least squares fits. The deviations of the $E_n = 169$ K points from the high E_n behavior is apparent and probably a manifestation of the onset of trapping.

where the constants a , b , and c are independent of both E_n and E_s . We have performed a global least squares fit of the data to Eq. (3) to determine the values of the coefficients a , b , and c . The bilinear fit to Eq. (3) has been carried out separately for each fine structure component and Table II lists the parameter values.

It is convenient to introduce the energy quantity $\langle E'_w \rangle = c/a$ as a parameter. Figure 8 presents the results of the global bilinear fit to the data using Eq. (1), i.e.,

TABLE II. Tabulation of the bilinear coefficients a , b , and $\langle E'_w \rangle (= c/a)$ determined for $E_n \geq 557$ K.

	F_1	F_2
a	0.088 ± 0.009	0.132 ± 0.005
b	0.180 ± 0.036	0.105 ± 0.019
$\langle E'_w \rangle$	2852 ± 448 K	2079 ± 154 K
χ^2	0.45	0.16

$\langle E_r \rangle = a(E_n + \langle E'_w \rangle) + bE_s$. In this figure we have plotted $\langle E_r \rangle / (E_n + \langle E'_w \rangle)$ against $E_s / (E_n + \langle E'_w \rangle)$ which according to Eq. (3) should be linear with slope b and intercept a . Only the $E_n \geq 557$ K data are used in this fit: the $E_n = 169$ K data are also displayed to point out their differences. As demonstrated in Fig. (5) the value of $\langle E_r \rangle$ for $E_n = 169$ K, $E_s = 750$ K is significantly higher than that for $E_n = 557$ K, $E_s = 750$ K. This obvious departure from the behavior predicted by Eq. (3) may indicate the onset of trapping or multiple collisions, which will be discussed later. Figure 8 demonstrates that the bilinear fit is quite good, as is also evidenced by the reduced χ^2 values listed in Table II. Note that the values of a , b , and $\langle E'_w \rangle$ differ for each spin-orbit component.

B. Fine structure excitation

We show in Fig. 9 and tabulated in Table III the measured $[\Omega = 3/2] / [\Omega = 1/2]$ population ratios as a function of E_s for the four values of E_n . The F_2/F_1 ratios were obtained by summing the populations given by the functions (a line when the rotational distributions are Boltzmann) determined by a least squares fit to the data over all rotational states to $J = 40.5$. As can be seen from this figure, the elec-

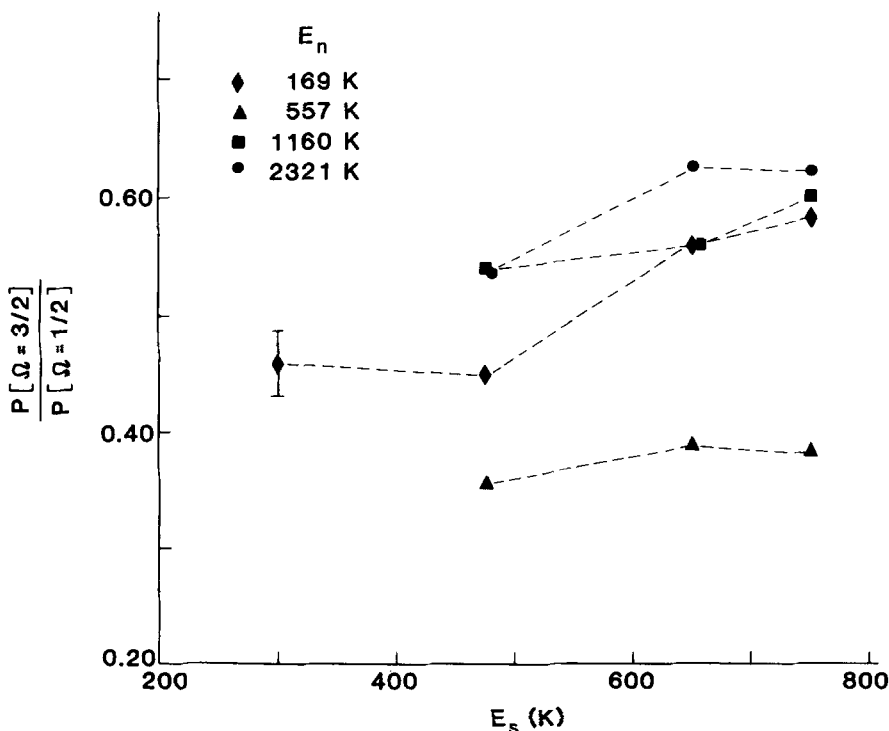


FIG. 9. Plot of the $[\Omega = 3/2] / [\Omega = 1/2]$ population ratios vs E_s for the four values of E_n employed. For $E_n \geq 557$ K the trend of increasing F_2 population with increasing E_n is observed, similar to the behavior observed for rotation. This trend is broken for the $E_n = 169$ K points, which have greater population ratios than their next highest, $E_n = 557$ K, counterparts.

TABLE III. $[\Omega = 3/2]/[\Omega = 1/2]$ population ratios averaged over 40 rotational levels tabulated against E_n and E_s .

E_n (K)	E_s (K)			
	300	475	650	750
169	0.459(0.071)	0.450(0.048)	0.559(0.068)	0.585(0.090)
557		0.354(0.042)	0.388(0.047)	0.383(0.045)
1160		0.540(0.020)	0.562(0.014)	0.602(0.012)
2321		0.535	0.629	0.623

tronic excitation shows a slight increase with E_s for the lowest beam energy but is nearly independent of E_s at all other E_n . Also to be noted is the fact that the population ratio is not simply an increasing function of E_n ; the $[\Omega = 3/2]/[\Omega = 1/2]$ ratio passes through a minimum at $E_n = 557$ K. The amount of excitation into the higher lying component is in all cases less than either the amount expected for total spin scrambling, $[\Omega = 3/2]/[\Omega = 1/2] = 1$, or for equilibrium to the surface temperature. The dependence of the F_2/F_1 population ratio on E_s and E_n is similar to that observed for $\langle E_r \rangle$, as demonstrated in Fig. 5. We have therefore attempted to describe the dependence of this ratio on E_s and E_n by the simple bilinear form of Eq. (1). To do this we introduce the electronic temperature, defined by

$$T_e \equiv -\Delta(3/2 - 1/2)/[k_b \ln(\text{Pop } 3/2/\text{Pop } 1/2)],$$

where $\Delta(3/2 - 1/2)$ is the 123 cm^{-1} spin-orbit splitting, k_b is the Boltzmann constant, and $\text{Pop } 3/2/\text{Pop } 1/2$ are the population ratios plotted in Fig. 9. The results, shown in Fig. 10, demonstrate that the three highest E_n data points can be fit to Eq. (1) but the fit is substantially poorer than that found for rotation (see Fig. 8). The best-fit values of the three previously defined coefficients are $a = 0.092(0.025)$, $b = 0.127(0.143)$, and $\langle E'_w \rangle = 790(822)$ K. The existence of a minimum in the

spin-component population ratio is not at all similar to the situation in gas phase collisions. We have recently found³⁵ that the electronic inelasticity follows rotation, both increasing monotonically with the total collision energy.

IV. DISCUSSION

A. Scattering mechanism

The rotational excitation measured in this work could, in principle, have contributions from both direct inelastic scattering and trapping-desorption scattering. As will be shown, direct inelastic scattering dominates the excitation observed along the specular direction. It is expected that any contribution from the trapping-desorption channel would be largest at the lowest beam energy if the adsorption step has no activation barrier. We have measured the angular distribution of NO by exciting the Q_1 bandhead ($J'' = 0.5-4.5$) for $E_n = 169$ K and have found that the scattered density near the specular direction is at least six times more intense than that found along the surface normal. For our detection geometry and with a $\cos \theta$ desorption angular dependence, the direct inelastic channel accounts for more than 90% of the specular density at $E_n = 169$ K.

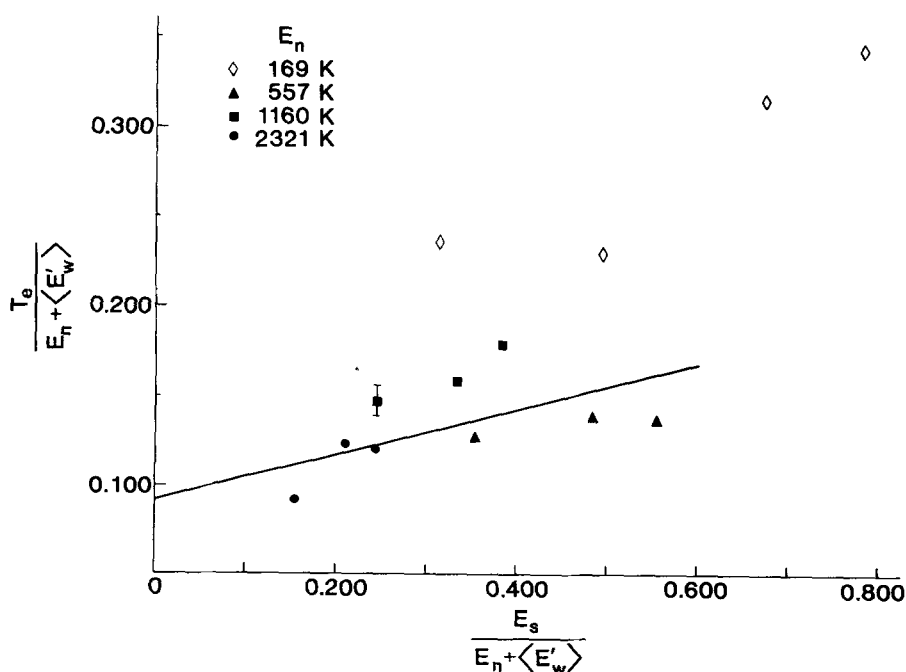


FIG. 10. Plot of the reduced variables $T_e/(E_n + \langle E'_w \rangle)$ vs $E_s/(E_n + \langle E'_w \rangle)$ assuming the same bilinear expression as that used for rotation but with different coefficient values. As rotation, only data points having $E_n \geq 557$ K were used in the bilinear least squares fit.

In the global bilinear fit to the data the $E_n = 169$ K points were not included. With one exception, the values of $\langle E_r \rangle$ for this E_n are higher than those expected for the direct inelastic channel [cf. Eq. (3)]. Furthermore, at $E_s = 300$ K, $\langle E_r \rangle > E_s$ for the F_2 component. Hence, no linear combination of direct inelastic and trapping/desorption (assuming $\langle E_r \rangle = E_s$) scattering channels can account for this behavior at $E_s = 300$ K. However, the $E_s > 300$ K data are consistent with the assumption that trapped molecules desorb with $\langle E_r \rangle = E_s$. These data are wholly inconsistent with the idea that $\langle E_r \rangle = E_s/2$ for the trapping/desorption channel predicted by a simple model³⁶ involving reduced adsorbate rotational dimensionality. This suggests that additional mechanisms such as incompletely accommodated multiple collisions are contributing to our observations. Therefore we conclude that the excitation we measure results predominantly from direct inelastic scattering. This is supported by the angular distribution measurements of Asada *et al.* for NO scattered from Ag(111).³⁷ For scattering conditions of $E_n = 800$ K and $T_s = 500$ K we estimate from their data that at most 5% of the specular density arises from trapping.

It might be tempting, nevertheless, to interpret the observed rotational distributions of Fig. 4 as arising from two channels, the low- J linear region from the trapping-desorption channel and the high- J non-Boltzmann region seen at $E_n = 2321$ K from the direct inelastic one. This interpretation would require a 50% contribution along the specular direction from the trapping-desorption channel, in contradiction to our observations. In addition, this interpretation would suggest that the direct inelastic channel contributes only at the highest beam energy. However, we observe that the rotational excitation depends on both the incident kinetic energy and the surface temperature at all beam energies studied. We stress that although our observations refer to direct inelastic scattering this does not exclude possible manifestations of trapping in the properties of molecules scattered in this channel. In Sec. IV C we estimate the fraction of incident molecules which are trapped.

B. Interpretation of the bilinear fit

The ability of Eq. (3) to describe the dependence of the mean final rotational energy on the two variables E_n and E_s allows us to draw several conclusions. The meaning of the coefficients a and b of Eq. (3) is clear; they represent respectively the fraction of the energy associated with E_n and the fraction associated with E_s which appear in the mean rotational excitation. In addition, we find a third constant, $\langle E_w' \rangle = c/a$, which adds to E_n and hence contributes a fixed amount to $\langle E_r \rangle$, independent of E_n and E_s . As will be discussed in the next section, $\langle E_w' \rangle$ can be associated with the NO/Ag(111) potential well depth averaged over all gas-surface geometries, denoted by $\langle E_w \rangle$.

From the form of Eq. (3) we conclude that the mean exit rotational energy scales linearly with both E_n and E_s . A linear scaling of this type has precedence in the gas-surface scattering literature.^{4(b)} It is observed in

the dependence of the mean final translational energy on E_n and E_s at fixed final exit angle. This result is characteristic of impulsive collisions in which the energy change occurs suddenly. Another conclusion is that $\langle E_r \rangle$ scales as the projection of the incident kinetic energy along the surface normal. These two conclusions are consistent with the assumptions underlying all simple, yet successful, one-dimensional impulsive (hard cube) models of atomic and molecular collisions at surfaces.

C. One-dimensional impulsive scattering models

We have employed a one-dimensional rotationally inelastic hard cube formalism^{38,39} in an effort to understand better the qualitative features of the final rotational state distributions and the values of the mean rotational energy parameter $\langle E_r \rangle$ used to characterize the rotational inelasticity. Hard cube models,⁴⁰ despite their inherent simplicity, have had considerable success in predicting qualitative trends in both the final angular distributions⁴¹ and final translational energy distributions^{4,42} in rare gas/surface scattering systems. There is now considerable experimental evidence which qualitatively supports one underlying assumption of the model, namely, the one-dimensional nature of the collision. These include helium diffraction³³ and inelastic argon scattering⁴ from similar close-packed metal surfaces. The second assumption, that of an impulsive interaction, undoubtedly leads to an overestimate of the inelasticity of the collision. This is usually compensated for by parametrizing the mass ratio which determines the energy exchange in an impulsive collision. This and the fact that the model does not account for surface recoil leads to an effective surface mass equal to 2–3 surface atoms. Certainly the assumptions of the model are approximate as evidenced by the observation of parallel momentum inelasticity,⁴ such as out-of-plane scattering.³⁷ Hence, it is generally recognized that the one-dimensional, impulsive approach engendered by the hard cube model cannot predict the detailed distributions of velocity, angle, or rotation and it is not our intention to compare quantitatively the predicted rotational population functions with those measured experimentally. However, given both the ability of the model to derive the general features of atom-surface scattering and the successful use of E_n as the scaling parameter in our own data, we seek to exploit the model to elucidate the bilinear behavior of $\langle E_r \rangle$ described by Eq. (3).

The potential in the hard cube model is one dimensional, perpendicular to the surface, and is composed of an attractive region and a repulsive wall. In the attractive part of the potential the surface is treated as motionless and infinitely massive as the interaction is long range and involves many surface atoms whose mean velocity is zero. Thus the acceleration (and subsequent deceleration after the collision) caused by the potential well is restricted to the gas molecule. In the repulsive (impulsive) part of the potential the surface is treated as a cube of finite mass with a distribution of velocities determined by the surface temperature. The diatomic gas molecule is represented by a hard ellipsoid which is assumed in this case to be initially rotationless.

The final relative velocity prior to deceleration by the attractive part of the potential v'_{rn} and final molecular angular velocity ω' for the impulsive collision are given by

$$\omega' = [2/(1+R)] [\mu_r R / K_y]^{1/2} v_{rn}, \quad (4a)$$

$$v'_{rn} = -[(1-R)/(1+R)] v_{rn}, \quad (4b)$$

where

$$R = \mu_r l^2 / K_y.$$

μ_r = The ratio of the reduced mass to the gas mass, i. e., $M_s / (M_s + M_g)$ where M_g is the gas mass and M_s is the surface mass.

μ = The ratio of the surface to gas mass, i. e., M_s / M_g .

l = The distance, resolved along the surface, between the ellipsoid surface contact point and the molecular center-of-mass.

K_y = The ratio of the ellipsoid moment of inertia to the gas mass.

v_{rn} = The initial normal component of the gas-surface relative velocity after acceleration by the attractive part of the potential.

Here, l is a function of the orientation of the ellipsoid at the moment of collision and R therefore contains all the orientation dependence in the model.

In a recent communication⁴³ we have described the general features of the final rotational state distributions, referred to as $P(E_r)$, predicted by this model for both zero and nonzero surface temperatures. We find:

(1) A classical rainbow singularity in $P(E_r)$ at $E_r = 0$ K. This is present even at finite surface temperatures although it is somewhat broadened.

(2) Possible rainbow singularities in $P(E_r)$ at $E_r \neq 0$ K when $E_s = 0$ K. At finite surface temperatures these are no longer classical singularities and appear as broad maxima in the $P(E_r)$ curves.

(3) A trapping cutoff of the highest rotational energy states due to the attractive potential well. As the surface temperature increases the sharpness of the cutoff decreases.

(4) Total alignment of the final rotational angular momentum parallel to the surface (excluding any initial

component of angular momentum perpendicular to the surface which is conserved in the collision). This is independent of surface temperature.

The combination of several averaging processes in addition to surface motion could account for the near Boltzmann behavior at low E_r and the presence of broad maxima in the $P(E_r)$ at high E_r . These averaging processes are manifested as a depolarization of the final angular momentum at low E_r ,⁹ and as out-of-plane scattering.³⁷ In addition, coupled channel calculations⁴⁴ show that the rainbow features are considerably broadened.

In order to compare the predictions of the model with the experimental results represented by Eq. (3) it is necessary to average $(\omega')^2$ over all possible initial orientations of the ellipsoid and initial surface (relative) velocities (where the averaging includes only those collisions which lead to direct inelastic scattering); this has been performed for flux in the Appendix where it is shown that $\langle E_r \rangle$ has a bilinear dependence on E_n and E_s . Further, because the experimental results reported here are density measurements, each final angular momentum state must be weighted by the corresponding final gas velocity obtained from Eq. (4b) after deceleration by the attractive part of the potential. This requires that the model be able to predict not only $\langle E_r \rangle$ but the correlation between the final translational and rotational energy as well. The one-dimensional assumption of the model gives rise to strong correlations between the translational and rotational degrees of freedom; i. e., the high final rotational states have correspondingly low final translational energy. However, the invariance of $\langle E_r \rangle$ with exit angle for the range of E_n used in these experiments and the weak dependence of the final translational energy with exit angle⁴¹ suggest that these correlations are being weakened by other averaging processes. We assume that any averaging process not taken into account by the simple model acts only to broaden the final rotational state distribution without appreciably altering the value of $\langle E_r \rangle$. This is tantamount to assuming that the averaging process is symmetric about $\langle E_r \rangle$. Finally, because $\langle E_r \rangle$ is independent of exit angle, we assume that although the experimental results are a differential measurement about specular they can be compared directly with the results of the model which represents an average over all exit angles. In contrast, at much higher E_n there is some dependence of $\langle E_r \rangle$ on exit angle.^{9(d)} The hard cube model would predict that a differential measurement about specular would lead to a lower value of $\langle E_r \rangle$ having a more pronounced dependence on E_s since higher rotational states exit at larger angles. With these considerations the mean final rotational energy in density space is given by

$$\frac{\langle E_r \rangle}{E_n + E_w} = \frac{1}{N} \int_0^\pi \sin \theta_e d\theta_e \frac{4\mu R}{(1+R)^2} \int_{v_{sc}(\theta_e)}^\infty \frac{(1 - v_s/v_n)^3 \exp\{-[\mu(E_n + E_w)/E_s](v_s/v_n)^2\} dv_s}{\{[(1 - 2\mu_r) + 2\mu_r(1+R)]^{-1}(v_s/v_n)\}^2 - v_w^2/v_n^2}^{1/2}}, \quad (5a)$$

$$N = \int_0^\pi \sin \theta_e d\theta_e \int_{v_{sc}(\theta_e)}^\infty \frac{(1 - v_s/v_n) \exp\{-[\mu(E_n + E_w)/E_s](v_s/v_n)^2\} dv_s}{\{[(1 - 2\mu_r) + 2\mu_r(1+R)]^{-1}(v_s/v_n)\}^2 - v_w^2/v_n^2}^{1/2}}, \quad (5b)$$

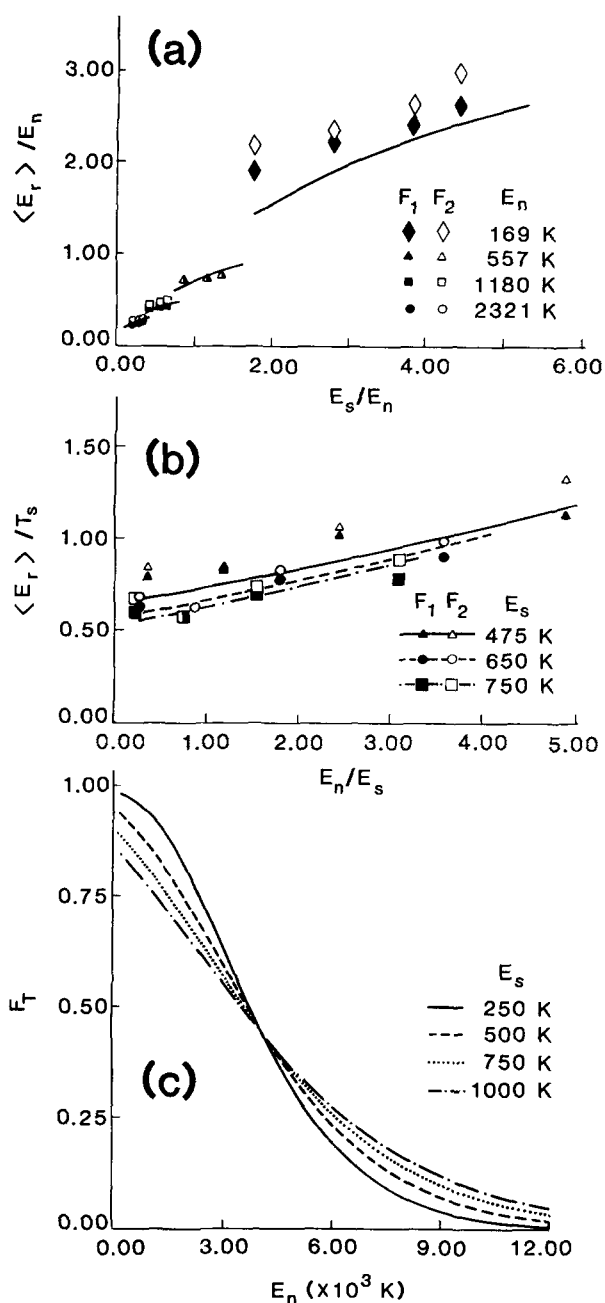


FIG. 11. Theoretical results obtained using the one-dimensional, impulsive hard cube model described in Section III C. The parameters used in the fit are: cube mass of 1.8 silver masses, gas-surface potential well depth of 3000 K, gas ellipsoid major and minor axes of 2.302 and 2.147 Å, respectively, with the center-of-mass offset from the geometric center of the ellipsoid 0.077 Å along the major axis. The calculated values for $\langle E_r \rangle$ are shown; (a) divided by E_n and plotted against E_s/E_n , and (b) divided by $T_s (\equiv E_s)$ and plotted against E_n/E_s . Also shown are the experimental data of Table I using the symbols defined in Figs. 6 and 7 for (a) and (b), respectively; (c) shows the dependence of the trapping probability on E_n at surface temperatures of 250, 500, 750, and 1000 K.

where E_w is the well depth, $v_n = -[2k_b(E_n + E_w)/M_g]^{1/2}$ is the gas velocity prior to the collision, v_s is the surface velocity, $v_w = [2k_b E_w/M_g]^{1/2}$, θ_e is the angle the major axis of the ellipsoid makes with the surface normal, and $v_{sc}(\theta_e)$ is the surface velocity that gives a final gas

velocity of zero, i.e., the value of v_s for which the denominators in Eqs. (5a) and (5b) vanish.

Equation (5a) was numerically fitted to the experimental data of Table I and the results are plotted in Fig. 11. The parameters for the calculation are, effective surface mass of $1.8 M_{Ag}$, $E_w = 3000$ K, ellipsoid major axis of 2.302 Å, and ellipsoid minor axis of 2.147 Å. Note that these are estimated parameters and are by no means determined by the data. In fact a comparable fit can be obtained for $1000 < E_w < 10000$ K by varying the other parameters.

At first glance it would appear that the model can reproduce the qualitative dependence of $\langle E_r \rangle$ on E_s [Fig. 11(a)] and E_n [Fig. 11(b)]. However, regardless of the particular parameters used, all sets of parameters that nominally reproduce the experimental data also predict very high trapping probabilities [Fig. 11(c)]. For instance, for $E_n = 2321$ K, $E_s = 650$ K, and using the parameters given above, the calculated fraction trapped is 67% rising to 87% for $E_n = 557$ K. The magnitude of the NO flux measured along the surface normal in angular distribution measurements for NO/Ag(111) scattering determined by Asada *et al.*³⁷ precludes trapping fractions greater than 36%. In fact, the experimental observation that $b > 0$ (i.e., $\partial \langle E_r \rangle / \partial E_s > 0$) can only be reproduced by the model when the fraction trapped is greater than 45% and is increasing as E_s decreases. In order to understand this point it is necessary to explain how trapping affects the value of $\langle E_r \rangle$ observed for direct inelastic scattering.

A particle will be trapped in the attractive well when the sum of the energy transferred to the surface and the energy transferred into the molecular internal degrees of freedom from E_n exceeds E_n . As demonstrated previously⁴³ molecules that have experienced large rotational excitations will be more likely to become trapped. Therefore, trapping leads to an apparent decrease in the value of $\langle E_r \rangle$ for the direct channel. In the hard cube model trapping increases with decreasing E_s only for $E_n \leq E_w$ where the fraction trapped is greater than 50%. For these conditions, $\langle E_r \rangle$ decreases with decreasing E_s (increasing fraction trapped) giving rise to $\partial \langle E_r \rangle / \partial E_s > 0$ as observed experimentally. In contrast, when $E_n > E_w$ the fraction trapped is less than 50% and increases with increasing E_s giving rise to $\partial \langle E_r \rangle / \partial E_s < 0$ contrary to the experimental results. We conclude that trapping causes the theoretical curves of Fig. 11(a) to be nonlinear at low E_s/E_n with positive slope, whereas the experimental results indicated by Eq. (3) are taken for conditions where there is little trapping. Thus the hard cube model is able to qualitatively reproduce the dependence of $\langle E_r \rangle$ on E_s and E_n but only by the use of parameters which lead to an unacceptably large trapping probability for the NO/Ag(111) system. However, Frankel *et al.*^{7(b)} have observed that for the system NO/graphite, where trapping is important the dependence of $\langle E_r \rangle$ on E_n deviates from linearity in the manner predicted by the model.

In view of the above results, it is apparent that the role of the attractive well in the model is twofold. First, it adds to the incident gas velocity normal to the surface

prior to the collision (and subtracts from the final gas velocity normal to the surface after the collision), which makes the incident energy normal to the surface look like $E_n + E_w$ and thereby increases the value of $\langle E_r \rangle$ for the direct channel. Second, it allows for the possibility of trapping which decreases the value of $\langle E_r \rangle$ for the direct channel. The relative importance of these two counteracting effects depends on the particular parameters used and on E_n and E_s . It is therefore not surprising that the data can be fit equally well by the hard cube model using a wide range of assumed well depths. Certainly, the fact that the theoretical curves in Fig. 11(a) are displaced toward higher $\langle E_r \rangle / E_n$ as E_s increases is a manifestation of the attractive part of the potential.

We wish to emphasize that the hard cube model assumes that molecules with more than one turning point in their normal momentum are trapped and hence are diffusely scattered at a later time. However, this assumption may overestimate the effects of trapping because some species undergoing multiple collisions may escape from the surface before complete equilibration, i. e., with a nondiffuse angular distribution and thereby contribute significantly to the species detected near specular. It is clear that an accurate comparison of the results indicated by Eq. (3) to the predictions of the impulsive model should include the contributions of multiple collisions to $\langle E_r \rangle$. However, it is doubtful if the cube assumption could accurately reproduce the surface response in a multiple collision event. Parallel momentum accommodation, inefficient on a single collision,⁴ can be expected to become important after several collisions. Recent results⁴⁵ utilizing a stochastic classical trajectory approach (generalized Langevin) have been able to reproduce the features of the $P(E_r)$ functions and the details of the velocity and angular distributions for NO/Ag(111). It would be interesting to see if such an approach could generate the functional form of Eq. (3) and at the same time give small trapping probabilities. Although we expect only minor qualitative differences between the two models for a direct collision, the Langevin technique may better describe multiple collision events.

D. Manifestations of the NO/Ag(111) potential

The results of the previous section demonstrate that in the limit of no trapping the quantity $\langle E'_w \rangle$ acts as an additive constant to E_n in causing rotational excitation. Since the trapping fraction at even the lowest E_n employed in this work has a limit of 36%, we believe our measurements correspond to a low trapping regime to which the limiting behavior applies. The fact that the model employed in the last section would predict deviation is not unexpected because the hard cube model is known to overestimate^{4,40,42} the extent of trapping.

Our values of $\langle E'_w \rangle$ (see Table II) should be compared to the value of 9076 K (0.78 eV) determined in the following manner by Kleyn *et al.*^{9(a)} They fit the Boltzmann region at low J to a temperature which was then extrapolated against E_n to yield an estimate of $\langle E'_w \rangle$. The distinction between the Boltzmann and rainbow regions in their data was more pronounced than ours be-

cause E_n ranges from 700 to 11 600 K. However, we believe this distinction between the Boltzmann and rainbow regions to be an artificial one for determining $\langle E'_w \rangle$. We question using any subset of the distribution applying to direct inelastic scattering to extract quantities characteristic of that channel. For example, the simple model of the preceding section (see also the Appendix) requires that the entire distribution must be considered. Moreover, the well depth obtained using the analysis of Kleyn *et al.*, which applies to the entire surface, might suggest the presence of much larger trapping fractions than inferred either in this study or the studies of Asada *et al.*³⁷

There is an additional determination of the NO/Ag(111) well depth, namely that of Goddard *et al.*⁴⁶ who obtained a value of 12 450 K (1.07 eV) by flash desorption. However, their value refers to NO surface sites that represent only 5% of the total number of Ag atoms available. Our measurements are insensitive to such possible minority sites. It should be noted that in general scattering experiments sample all possible surface sites while in desorption only a restricted sample of sites is probed.

Closer inspection of Table I shows that the $\langle E_r \rangle$ associated with the F_2 component is generally larger than that of the F_1 component. The difference between these two quantities increases with E_n above $E_n = 557$ K. As a result, the best least squares values of a , b , and $\langle E'_w \rangle$ (Table II) differ for each spin-orbit component outside of their combined uncertainties. We are unable to establish at present the cause of this behavior. Several possibilities could at least partially account for these observations. In the gas-phase literature there is precedence that $\Delta\Omega = 1$ transitions become more probable as the final J increases. This behavior is seen^{24,35} for collisions of NO $^2\Pi_{1/2,3/2}$ with Ar, and this phenomenon has been predicted by Chu⁴⁷ who finds the relative cross sections for $[\Delta\Omega = 1]/[\Delta\Omega = 0]$ transitions scale with the square of the Hund's case (a) F_1 and F_2 mixing coefficients appropriate to the true, intermediate state for each J . Using these J -dependent mixing coefficients and considering only the first two terms in the multipole expansion of the potential, the predicted $[\Delta\Omega = 1]/[\Delta\Omega = 0]$ cross section ratio for NO increases by nearly a factor of 10 from $J - J' = 5.5$ to $J - J' = 25.5$. Although the situation for surface scattering is likely to be considerably more complex, the result suggests that higher values of $\langle E_r \rangle$ are not unexpected in the F_2 component. If this is true then the high rotational states of the F_1 component would be lost preferentially to the F_2 component. This mechanism might be incorporated in Eq. (3) by simply adding to the expression for $\langle E_r \rangle$ for the F_2 component and subtracting the same term for the F_1 component, where d is a constant. This would preserve the bilinear dependence of $\langle E_r \rangle$ on E_n and E_s and predicts that both $a(3/2)$ and $b(3/2)$ in Table II should be greater than $a(1/2)$ and $b(1/2)$. The data only partially bear this out. Another problem is that this model cannot account for $\langle E'_w \rangle(1/2) \neq \langle E'_w \rangle(3/2)$. Specifically, the best least squares values of $\langle E'_w \rangle$ differ by nearly 800 K, which lies outside their combined uncertainties by 200 K. This difference corresponds to 37% of the F_1 value. We

also note that such a splitting is more than 4 ± 2 times larger than the splitting of the F_1 and F_2 components in the isolated molecule and may be indicative of different $\text{NO}(^2\Pi_{1/2,3/2})/\text{Ag}(111)$ potentials. However, this picture may be complicated by several factors. First, the incident beam is over 98% in the F_1 component. To be affected by a different potential well would require a transition from F_1 to F_2 in the entrance channel. In addition, for this difference between the two wells to be manifested in the final rotational state distributions, a differential transition probability between the two components would be required in the exit channel. Further experiments which address the subtle differences between the two fine structure components are needed.

E. Conclusion

Using the technique of laser induced fluorescence we have measured the rotationally and electronically inelastic scattering of NO from clean Ag(111). The incident NO molecules were rotationally and translationally relaxed to <10 K and more than 98% of the molecules were in the lowest ($^2\Pi_{1/2} = F_1$) spin-orbit component. This allows unambiguous determination of the extent of rotational and electronic excitation upon collision. The NO internal state distribution was monitored as a function of incident kinetic energy, surface temperature, and incident scattering angle. At low incident kinetic energies the rotational state distributions appear Boltzmann but at higher incident kinetic energies a broad maximum appears at high J . We have determined that the measured excitation is a result of direct inelastic scattering and that the average final rotational energy $\langle E_r \rangle$ depends linearly on both the normal component of the incident kinetic energy, and the surface temperature $E_s (= T_s)$:

$$\langle E_r \rangle = a(E_n + \langle E'_w \rangle) + bE_s.$$

Here a , b , and $\langle E'_w \rangle$ are constants independent of E_n and E_s for $557 < E_n < 2321$ K and $475 < E_s < 750$ K. This conclusion applies to the first moments obtained by averaging over the entire final rotational state distribution, i. e., both the low- J Boltzmann region and the high- J rainbow region are included. Our lowest beam energy data ($E_n = 169$ K) show a similar linear dependence on E_s but the slope is larger than b and the intercept is lower than that obtained by extrapolating the $E_n \geq 557$ K data [using $a(169 \text{ K} + \langle E'_w \rangle)$]. We interpret $\langle E'_w \rangle$ as a consequence of the true averaged NO/Ag(111) well depth. Efficient excitation of the F_2 component is found and its

value of $\langle E_r \rangle$ exceeds that of the F_1 component for $E_n > 557$ K. Thus, the two fine structure distributions yield somewhat different values for a , b , and $\langle E'_w \rangle$, suggesting possibilities of J -dependent $\Delta\Omega$ electronic inelasticity and differences in the two $\text{NO}(^2\Pi_{1/2,3/2})/\text{Ag}(111)$ potentials. On the other hand, the $\langle E_r \rangle$ values for the different $\text{NO } ^2\Pi \Lambda$ doublets corresponding to different orientations of the π electron cloud are found to be the same within experimental uncertainty, although differences have been measured by Kleyn *et al.*^{9(c)} at higher incident beam energies. We also find that the population of the F_2 component relative to the F_1 component increases near $E_n = 169$ K. This trend parallels that found for $\langle E_r \rangle$. It is quite likely, given the departures from simple hard cube behavior found at $E_n = 169$ K, that these effects represent a trend toward equilibration to T_s . This view is also supported by the fact that both $\langle E_r \rangle$ and the population ratio at this beam energy exhibit a more pronounced dependence on surface temperature than do the corresponding values at higher E_n . Whether this is the result of the classically expected phenomenon of multiple encounters with the surface is uncertain.

The bilinear dependence of $\langle E_r \rangle$ on E_n and E_s can be approximated using a one-dimensional impulsive model for the mean rotational energy density. However, this fit requires a trapping fraction larger than that inferred from angular distributions.³⁷ The hard cube model assumes that all collisions having more than one turning point belong to the trapping/desorption channel. It may be necessary to consider models which include incompletely accommodated multiple collisions.

ACKNOWLEDGMENTS

We wish to thank Greg Sitz for valuable assistance. G. D. K. thanks Stanford University for the Grace Fellowship in Chemistry and R. N. Z. thanks the Shell Companies Foundation, Inc. for a Shell Distinguished Chair. This work was supported in part by the Office of Naval Research under N00014-78-C-0403 and the Army Research Office under DAAG-29-80-K-0035.

APPENDIX

It is possible to show that under certain limited conditions the mean final rotational energy flux predicted by the hard cube formalism described in Sec. IV C depends on E_n and E_s in a bilinear fashion similar to that given by Eq. (3). The expression for $\langle E_r \rangle$ in flux space, denoted by $\langle E_r \rangle_f$, is given by

$$\frac{\langle E_r \rangle_f}{E_n + E_w} = \frac{1}{N} \int_0^\pi \sin \theta_e d\theta_e \frac{4\mu R}{(1+R)^2} \int_{v_{sc}(\theta_e)}^\infty (1 - v_s/v_n)^3 \exp\{-[\mu(E_n + E_w)/E_s](v_s/v_n)^2\} dv_s, \quad (\text{A1})$$

$$N = \int_0^\pi \sin \theta_e d\theta_e \int_{v_{sc}(\theta_e)}^\infty (1 - v_s/v_n) \exp\{-[\mu(E_n + E_w)/E_s](v_s/v_n)^2\} dv_s, \quad (\text{A2})$$

where the various constants have been defined in connection with Eqs. (4) and (5). This equation can be simplified by introducing the assumption that the critical surface velocity for trapping, $v_{sc}(\theta_e)$, be small enough

so that all surface velocities having significant probability at a given E_s lead to direct inelastic scattering. This requires that $v_{sc}(\theta_e) \lesssim 3(2k_b E_s/M_s)^{1/2}$. This criterion is met when the incident velocity for the gas after

acceleration by the attractive part of the potential is large compared to the surface cube velocity, i. e., when $\mu(E_n + E_w)/E_s \gg 1$. In this case the lower limit of the integral over surface velocities in Eqs. (A1) and (A2) can be extended to minus infinity.

Because the expression for the final angular velocity [cf. Eq. (4)] is separable in the angular and surface velocity variables and because the lower limit of the surface velocity integral in Eqs. (A1) and (A2) is assumed to be independent of the angular variable, it follows that the expression for the mean final rotational energy flux [Eq. (A1)] is separable in the θ_e and v_s variables and can therefore be expressed as the product of two factors. The first factor, given by the integral over molecular orientation θ_e , and represented by the symbol $\langle A_1 \rangle$, contains all the dependence of $\langle E_r \rangle_f$ on the "shape" or geometry of the gas molecule:

$$\langle A_1 \rangle = \frac{1}{2} \int_0^\pi \frac{4\mu_e R}{(1+R)^2} \sin \theta_e d\theta_e. \quad (\text{A3})$$

The second factor, given by the integral over surface velocities, contains all the dependence of $\langle E_r \rangle_f$ on the energies in the system, E_n , E_w , and E_s . Performing the integration over surface velocity gives for $\langle E_r \rangle_f$:

$$\langle E_r \rangle_f = \langle A_1 \rangle \left\{ (E_n + E_w) + \frac{3}{2\mu} E_s \right\}. \quad (\text{A4})$$

This bilinear form for the mean rotational energy flux is of the same form as Eq. (3) which represents the experimentally observed relationship for the mean rotational energy density.

When Eq. (A4) is applicable, then the constants in the bilinear fit have an appealing interpretation, namely, $a_f = \langle A_1 \rangle$ describes the shape of the molecule as seen by the surface, $b_f = 1.5 \langle A_1 \rangle / \mu$ permits the extraction of the effective surface mass, i. e., the "number" of surface atoms interacting with the gas, and $c_f = \langle A_1 \rangle E_w$ is related to the average well depth. These conclusions hold for the hard cube model but retain their validity if the final angular velocity ω' is proportional to the normal component of the initial relative velocity v'_m .

¹S. T. Ceyer and G. A. Somorjai, *Annu. Rev. Phys. Chem.* **28**, 477 (1977).

²J. C. Tully, *Annu. Rev. Phys. Chem.* **31**, 319 (1980).

³M. J. Cardillo, *Annu. Rev. Phys. Chem.* **32**, 331 (1981).

⁴(a) J. Lapujoulade and Y. Lejay, *J. Chem. Phys.* **63**, 1389 (1975); (b) J. E. Hurst, Jr., L. Wharton, K. C. Janda, and D. J. Auerbach, *J. Chem. Phys.* **78**, 1559 (1983); K. C. Janda, J. E. Hurst, Jr., C. A. Becker, J. P. Cowin, D. J. Auerbach, and L. Wharton, *ibid.* **72**, 2403 (1980); (c) H. Asada and T. Matsui, *Jpn. J. Appl. Phys.* **21**, 259 (1982); (d) J. C. Tully, *Acc. Chem. Res.* **14**, 188 (1981); (e) *Surf. Sci.* **111**, 461 (1981).

⁵(a) H. Hoinkes, *Rev. Mod. Phys.* **52**, 933 (1980); (b) M. W. Cole, D. R. Frankl, and D. L. Goodstein, *ibid.* **53**, 199 (1981).

⁶See, for example, the Diffraction and Structure section of Ref. 3 and references cited therein.

⁷(a) F. Frenkel, J. Häger, W. Krieger, H. Walther, C. T. Campbell, G. Ertl, H. Kuipers, and J. Segner, *Phys. Rev. Lett.* **46**, 152 (1981); (b) F. Frenkel, J. Häger, W. Krieger, H. Walther, G. Ertl, J. Segner, and W. Vielhaber, *Chem. Phys. Lett.* **90**, 225 (1982); (c) G. Ertl, H. Robota, J. Seg-

ner, W. Vielhaber, F. Frenkel, J. Häger, W. Krieger, and H. Walther, *Surf. Sci.* (to be published).

⁸G. M. McClelland, G. D. Kubiak, H. G. Rennagel, and R. N. Zare, *Phys. Rev. Lett.* **46**, 831 (1981).

⁹(a) A. W. Kleyn, A. C. Luntz, and D. J. Auerbach, *Phys. Rev. Lett.* **47**, 1169 (1981); (b) *J. Chem. Phys.* **76**, 737 (1982); (c) *Phys. Rev. B* **25**, 4273 (1982); (d) *Surf. Sci.* **117**, 33 (1982).

¹⁰(a) M. Asscher, W. L. Guthrie, T.-H. Lin, and G. A. Somorjai, *Phys. Rev. Lett.* **49**, 76 (1982); (b) *J. Chem. Phys.* **78**, 6992 (1983).

¹¹H. Zacharais, M. M. T. Loy, and P. A. Roland, *Phys. Rev. Lett.* **49**, 1790 (1982).

¹²J. S. Hayden and G. J. Diebold, *J. Chem. Phys.* **77**, 4767 (1982).

¹³(a) G. Boato, P. Cantini, and L. Mattera, *Jpn. J. Appl. Phys. Suppl.* **2**, Part 2, 555 (1974); (b) R. G. Rowe and G. Ehrlich, *J. Chem. Phys.* **62**, 735 (1975); **63**, 4648 (1975); (c) W. Allison and B. Feuerbacher, *Phys. Rev. Lett.* **45**, 2040 (1981); (d) G. Brusdeylins and J. P. Toennies, *Surf. Sci.* **126**, 647 (1983).

¹⁴J. P. Cowin, C. F. Yu, S. J. Sibener, and J. E. Hurst, Jr., *J. Chem. Phys.* **75**, 1033 (1981).

¹⁵J. W. Hepburn, F. J. Northrup, G. L. Ogram, J. C. Polanyi, and J. M. Williamson, *Chem. Phys. Lett.* **85**, 127 (1982).

¹⁶D. Ettinger, K. Honma, M. Keil, and J. C. Polanyi, *Chem. Phys. Lett.* **87**, 413 (1981).

¹⁷J. B. Cross and J. J. Valentini, 3rd International Conference on Vibrations at Surfaces, 1982.

¹⁸R. R. Cavanagh and D. S. King, *Phys. Rev. Lett.* **47**, 1829 (1981).

¹⁹D. Mantell, S. Ryali, B. L. Halpern, G. L. Haller, and J. B. Fenn, *Chem. Phys. Lett.* **81**, 185 (1981).

²⁰S. L. Bernasek and S. R. Leone, *Chem. Phys. Lett.* **84**, 401 (1981).

²¹J. Misewich, C. N. Plum, G. Blyholder, P. L. Houston, and R. P. Merrill, *J. Chem. Phys.* **78**, 4245 (1983).

²²D. E. Tevult, L. D. Talley, and M. C. Lin, *J. Chem. Phys.* **72**, 3314 (1980).

²³R. P. Thorman and S. L. Bernasek, *J. Chem. Phys.* **74**, 6498 (1981).

²⁴(a) N. Zacharais, M. M. T. Loy, P. A. Roland, and A. Sudbø, *Appl. Phys. B* **28**, 113 (1982); (b) P. Andersen, M. H. Alexander, H. Joswig, and H. Pauly, (to be published).

²⁵(a) K. R. German, R. N. Zare, and D. R. Crosley, *J. Chem. Phys.* **54**, 4039 (1971); (b) E. M. Weinstock, R. N. Zare, and L. A. Melton, *ibid.* **56**, 3456 (1972).

²⁶R. L. Byer and M. D. Duncan, *J. Chem. Phys.* **74**, 2174 (1981).

²⁷J. A. Serri, M. J. Cardillo, and G. E. Becker, *J. Chem. Phys.* **77**, 2175 (1982).

²⁸P. R. R. Langridge-Smith, E. Carrasquillo M., and D. H. Levy, *J. Chem. Phys.* **74**, 6513 (1981).

²⁹M. G. Littman, *Opt. Lett.* **3**, 138 (1978).

³⁰J. Morabito, R. Steiger, R. Muller, and G. A. Somorjai, *Structure and Properties of Solid Surfaces*, edited by G. A. Somorjai (Wiley, New York, 1969), pp. 50-51.

³¹Calculated from spectroscopic constants; see R. N. Zare, *Molecular Spectroscopy: Modern Research* (Academic, New York, 1972), p. 207.

³²We use the symbol E_s to denote the mean kinetic energy of the surface atoms normal to the surface. This is equal to T_s for a Boltzmann distribution of surface atom velocities. Note that this definition of E_s differs from that used to describe the mean kinetic energy expected for a gas in equilibrium with a surface at T_s , namely $E_g = 2T_s$.

³³(a) G. Boato, P. Cantini, and R. Tatarek, *J. Phys. F* **6**, L237 (1976); (b) J. M. Horne and D. R. Miller, *Surf. Sci.* **66**, 365 (1977); (c) G. Boato, P. Cantini, and R. Satarek, in *Proceedings of the Seventh International Vacuum Congress and Third International Conference on Solid Surfaces* (Vienna, 1977), Vol. 2, p. 1377; (d) J. H. Horne, S. C. Yerkes, and D. R.

- Miller, Surf. Sci. **93**, 47 (1980).
- ³⁴R. Laughlin, Phys. Rev. B **25**, 2222 (1982).
- ³⁵G. D. Kubiak, J. E. Hurst, Jr., and R. N. Zare (unpublished results).
- ³⁶S. E. Bialkowski, J. Chem. Phys. **78**, 600 (1983).
- ³⁷(a) H. Asada, and T. Matsui, Jpn. J. Appl. Phys. **21**, 259 (1982); (b) **19**, 2055 (1980); **20**, 527 (1981); (c) Surf. Sci. **110**, 270 (1981).
- ³⁸J. D. Doll, J. Chem. Phys. **59**, 1038 (1973).
- ³⁹(a) W. L. Nichols and J. H. Weare, J. Chem. Phys. **62**, 2754 (1975); (b) **63**, 279 (1975); (c) **66**, 1075 (1977).
- ⁴⁰R. M. Logan and R. E. Stickney, J. Chem. Phys. **44**, 195 (1966).
- ⁴¹A. Stoll, D. Smith, and R. Merrill, J. Chem. Phys. **51**, 163 (1971).
- ⁴²E. K. Grimmelmann, J. C. Tully, and M. J. Cardillo, J. Chem. Phys. **72**, 1039 (1980).
- ⁴³J. E. Hurst, Jr., G. D. Kubiak, and R. N. Zare, Chem. Phys. Lett. **93**, 235 (1982).
- ⁴⁴J. A. Barker, A. W. Kleyn, and D. J. Auerbach, Chem. Phys. Lett. **97**, 9 (1983).
- ⁴⁵J. C. Tully (private communication).
- ⁴⁶P. J. Goddard, J. West, and R. M. Lambert, Surf. Sci. **71**, 447 (1978).
- ⁴⁷S. Chu, Astrophys. J. **206**, 640 (1976).